JOURNAL OF GUIDANCE, CONTROL, AND DYNAMICS
Vol. 23, No. 5, September–October 2000

Transonic Flutter Suppression Control Law Design and Wind-Tunnel Test Results

Vivek Mukhopadhyay*
NASA Langley Research Center, Hampton, Virginia 23681-2199

Flutter suppression control law design and wind-tunnel test results in transonic flow for a NACA 0012 wing model, under the benchmark active control technology program at NASA Langley Research Center, will be presented. Two control law design processes using classical and minimax techniques are described. Design considerations for improving the multivariable system robustness are outlined. The classical control law was digitally implemented and tested in the NASA Langley Transonic Dynamics Tunnel. In wind-tunnel tests in air and heavy gas medium, the closed-loop flutter dynamic pressure was increased by over 50% up to the wind-tunnel upper limit. The active flutter suppression system also provided significant robustness, relative to gain and phase perturbations, even in the presence of transonic shocks and flow separation.

Nomenclature

$\boldsymbol{A}_0$ = controller state matrix
a = rate filter parameter
$\boldsymbol{B}_0$ = minimax estimator gains
$\boldsymbol{C}_o$ = constant optimal feedback gains
$\boldsymbol{D}_0$ = minimax estimator gain component
d = differential operator
$\boldsymbol{E}$ = output noise distribution matrix
$\boldsymbol{F}$ = plant state dynamics matrix
$\boldsymbol{G}$ = plant input matrix
$\boldsymbol{G}(s)$ = plant transfer function
g = acceleration due to gravity
$\boldsymbol{H}$ = plant output matrix
$\boldsymbol{I}$ = identity matrix
J = quadratic performance index
KP = pitch position gain factor
KR = pitch rate gain factor
$\boldsymbol{K}(s)$ = controller transfer function
$\boldsymbol{P}$ = estimator error covariance matrix
$\boldsymbol{Q}$ = design weighting matrices
q_{flutter} = open-loop flutter dynamic pressure
$\boldsymbol{R}$ = noise weighting matrices
$\boldsymbol{S}$ = symmetric positive definite matrix
s = Laplace operator
t = time
$\boldsymbol{u}$ = control input vector
W = noise constraints
$\boldsymbol{w}$ = disturbance input vector
$\boldsymbol{X}$ = state covariance matrix
$\boldsymbol{x}$ = plant state vector
$\boldsymbol{y}_d$ = design output vector
$\boldsymbol{y}_s$ = sensor output vector
$\boldsymbol{z}$ = minimax controller state vector
zle = leading-edge accelerometer output
zte = trailing-edge accelerometer output
α = eigenvalue shift factor
γ = scalar parameter for minimax design
$\boldsymbol{\Delta}$ = uncertainty block transfer function
δte = trailing-edge control surface deflection
$\boldsymbol{\Lambda}$ = stable subspace eigenvector of λ
$\boldsymbol{\lambda}$ = Lagrange multiplier
ρ = spectral radius
$\underline{\sigma}$ = minimum singular value
ϕ = phase margin
ω = frequency

Subscripts

com = command input
d = design
o = optimal value
s = sensor
u = input
v = sensor noise
w = plant input noise
y = output

Superscripts

T = transpose
-1 = inverse

Introduction

THE benchmark active controls technology (BACT) and wind-tunnel test program at NASA Langley Research Center was started with the objective of investigating the nonlinear unsteady aerodynamics and active flutter suppression of standard wings in transonic flow.[1–4] Under the initial wind-tunnel test program, a rectangular wing with NACA 0012 airfoil cross section was constructed and equipped with pressure transducers, active trailing-edge control surface, and two spoilers. The model was mounted on a pitch and plunge apparatus in the NASA Transonic Dynamics Tunnel and was designed to flutter in transonic flows with oscillating shocks and boundary-layer separation. Because of the complex nature of transonic flow, it was necessary to develop a robust flutter suppression system that would be stable under these flow conditions. This paper describes two flutter suppression control law design processes using classical and minimax techniques. Both designs were based on a set of linear analytical models and experience gained from previous flutter suppression test programs.[5–7] The wind-tunnel model and preliminary analysis are described first followed by the classical control law design process. Procedures for evaluating and improving the singular-value-based multivariable system robustness[8,9] are then described. Next, a robust control law design process using a unified linear quadratic Gaussian and minimax method[10–14] is presented. Finally, a summary of the wind-tunnel test results using the classical control law is described and compared with analytical predictions.

Presented as Paper 99-1396 at the AIAA/ASME/ASCE/AHS/ASC 40th Structures, Structural Dynamics, and Materials Conference and Exhibit, St. Louis, MO, 12–15 April 1999; received 24 May 1999; revision received 4 February 2000; accepted for publication 7 February 2000.

*Senior Aerospace Engineer. Associate Fellow AIAA.

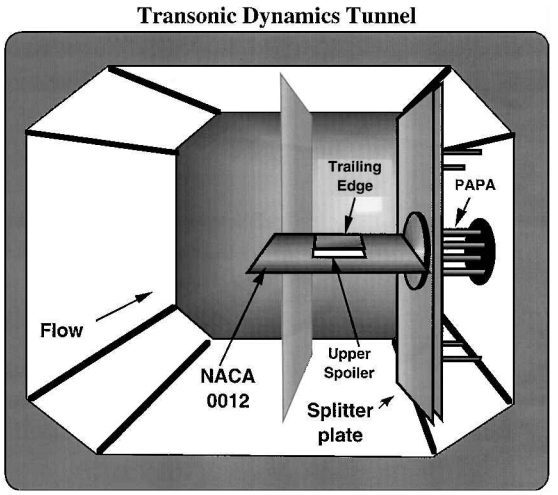

Fig. 1 BACT model test setup in wind tunnel.

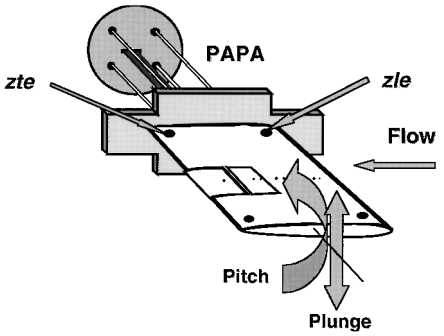

Fig. 2 NACA 0012 BACT wing on PAPA.

Wind-Tunnel Model Description

A perspective view of the BACT model[1,2] mounted on the pitch and plunge apparatus[3,4] (PAPA) in the wind tunnel is shown in Fig. 1. This PAPA mechanism was separated from the primary flow by a long splitter plate and allowed the rigid wing to have vertical (plunge) and rotational (pitch) degrees of freedom about the mid-chord at known frequencies. The plunge and pitch frequencies of the PAPA mounted NACA 0012 wing model were set at 3.3 and 5.2 Hz, respectively. Locations of four accelerometer sensors and the trailing-edge control surface are shown in Fig. 2. Two accelerometer sensors were located near the wing leading edge *zle* and trailing edge *zte* at the section inboard. An identical pair of sensors was located at the wing outboard section, as a spare. The active trailing-edge control surface was operated by a closed-loop electrohydraulic actuator and was used as flutter control input, as described here. A pair of active spoilers was also located on the upper and lower surfaces, just ahead of the trailing-edge control surface. Reference 15 describes application of the spoilers for BACT flutter suppression. Each of the control surfaces stretched over 30% of the span and 25% of the chord. The preliminary analysis and classical control law design process are described next.

Preliminary Analysis

The preliminary analysis, control surface sizing, and flutter suppression control law design were based on analytical state-space equations of motion of the BACT wing model.[1–4] These linear equations were developed analytically, using structural dynamic analysis and unsteady doublet lattice aerodynamics with rational polynomial approximations.[5] These state-space equations consisted of 14 states, 2 design inputs, and 7 design outputs. The 14 states represent plunge, pitch, plunge rate, pitch rate, 3 aerodynamic states for plunge, 3 aerodynamic states for pitch, 2 trailing-edge flap actuator states, and 2 Dryden gust states, respectively. The two inputs are the trailing-edge flap actuator command δte_{com} and gust input noise. The seven outputs are *zte* and *zle* acceleration, trailing-edge flap command, trailing-edge flap deflection δte, deflection rate, acceleration, and gust velocity. These 14th-order state-space equations were used for classical control law design and for performance simulation and verification purposes. For minimax control law design purposes, the 14th-order state-space equations were reduced to fourth-order state-space equations, using residualization and Schur's balanced reduction method.[6,7] First, it was reduced to an eighth-order system using a residualization technique, in which only the static part of all modes above 15 Hz were retained. The resulting eighth-order system was then balanced and the four states of the system with largest balanced singular values were retained.

Open-Loop Responses

In an air medium, the analytical open-loop flutter dynamic pressure q_{flutter} was near 128 psf. In heavy gas, the analytical flutter dynamic pressure was close to 150 psf. The flutter frequency was near 4.2 Hz. Figure 3 shows the response of the wing trailing- and leading-edge accelerometers, lift force, and pitching moment due to a 1-deg step command of the trailing-edge control surface, in air at 225 psf dynamic pressure. The resulting initial acceleration is of the order 0.05 *g*. This motion is primarily vertical plunge motion, mixed with small pitch response. The oscillatory lift force diverges rapidly at a rate of 6 lb/s. The pitching moment diverges at a rate of about 1 lb/s.

Frequency Responses

The open-loop frequency responses were studied using this 14th-order plant model, in air at 225 psf, to select a possible candidate for the best feedback signal for active flutter suppression. Bode diagrams of the trailing- and leading-edge accelerometers *zte* and *zle* and their difference (*zte* − *zle*) due to the trailing-edge control surface excitation δte are shown in Fig. 4. Magnitude plots of *zte* and *zle* indicate predominant plunge response at 3.3-Hz excitation

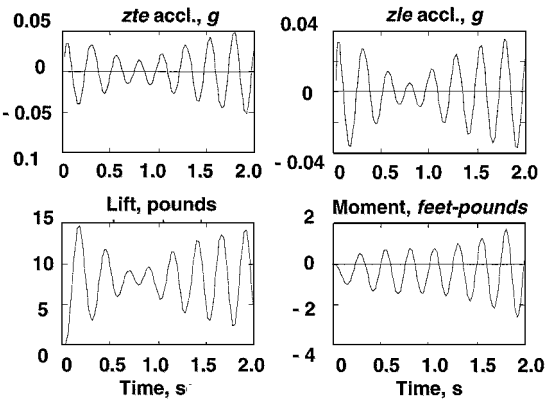

Fig. 3 Open-loop time responses to unit step δte_{com} in air at 225 psf, Mach 0.5.

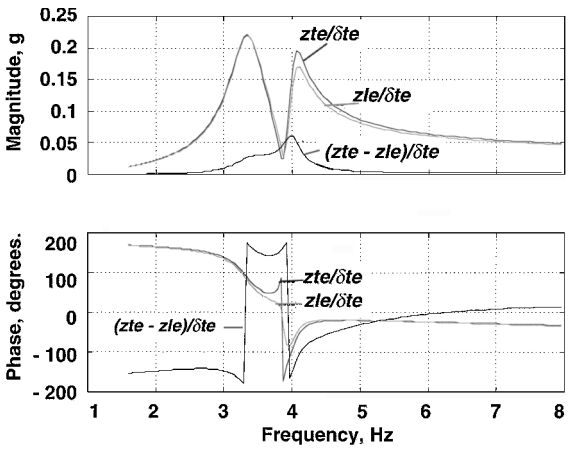

Fig. 4 Bode diagrams of *zte* and *zle* and *zte* − *zle* due to δte excitation, in air at 225 psf.

frequency. At 4.2-Hz excitation, the motion is a combination of pitch and plunge with pitch motion leading the plunge. Their difference ($zte - zle$) represents a signal proportional to the pitch acceleration and can be integrated to provide a pitch-rate proportional feedback. Figure 4 shows that the magnitude of this $zte - zle$ signal is small and peaks at flutter frequency to about 0.05 g/deg. Feedback of this signal with a high gain could provide maximum pitch damping at the flutter frequency.

Classical Control Law Design

Based on this Bode plot analysis, a classical flutter suppression scheme using pitch-rate proportional feedback signal from $zte - zle$ was first developed. The Nyquist diagram of $zte - zle$ due to the trailing-edge control surface excitation δte in air at 200 psf is shown in Fig. 5a. The arrow indicates increasing frequency of excitation from 2 to 6 Hz, with each asterisk representing frequency increment of 1 rad/s. Because the open-loop plant model had a pair of complex unstable poles, and the Nyquist contour did not encircle the -1 point, the unit feedback closed-loop system would be unstable. To achieve Nyquist stability, the $zte - zle$ signal was integrated to provide a 90-deg phase lag and then used for feedback with sufficiently high gain. Thus, the Nyquist contour would rotate 90 deg clockwise and then expand to encircle the -1 point to indicate a stable linear system.

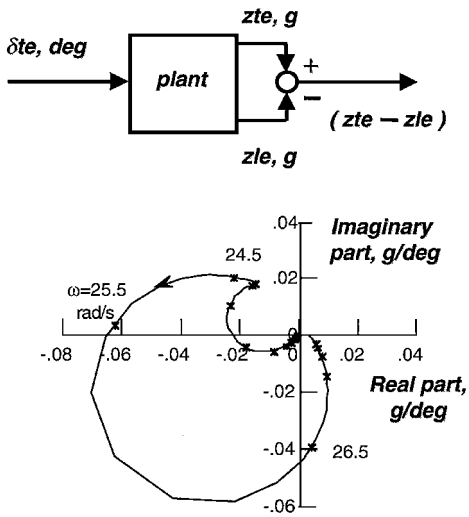

Fig. 5a Nyquist diagram of $zte - zle$ due to δte excitation, in air at 200 psf.

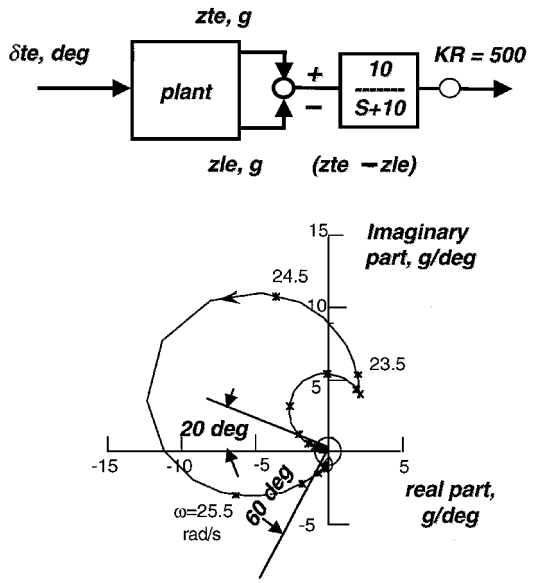

Fig. 5b Nyquist diagram of $zte - zle$ with $10/(s+10)$ lag filter and a gain $KR = 500$, due to δte excitation, in air at 200 psf.

Instead of using a pure integrator $1/s$, a first-order lag filter of type $a/(s + a)$ was used, to avoid amplification of any static bias. The filter parameter a and feedback gain selection processes are described next.

Gain Selection

Two first-order lag filters, $5/(s + 5)$ and $10/(s + 10)$, were examined. The latter was selected to achieve a higher phase margin at the plant input above the flutter frequency. Higher phase margin was desirable, to compensate for phase lag effects of antialiasing filters, computational delay, and the actuator.[6,7] The 25-Hz antialiasing filter and the 1/200 s computational delay contribute about 20 deg of phase lag at the flutter frequency. Moreover, with increasing dynamic pressure, the actuator may have an additional unknown phase lag because the control surface moves against higher aerodynamic loads. The Nyquist diagram of the $zte - zle$ signal with $10/(s + 10)$ lag filter and a feedback gain $KR = 500$, due to the trailing-edge control surface excitation δte, in air at 200 psf, is shown in Fig. 5b. The unit circle is also shown. With this feedback gain, the Nyquist contour encircles the -1 point, indicating that the closed-loop system is stable. As desired, the phase margin at the plant input above the flutter frequency was about 60 deg, but the phase margin below the flutter frequency was only 20 deg. Preliminary analysis indicated that this basic simple control law 1

$$\delta te = 500[10/(s + 10)](zte - zle) \tag{1}$$

could suppress the flutter instability in the dynamic pressure range from 0 to over 225 psf, both in air and in a heavy gas medium. However, the closed-loop damping and stability margins required substantial improvement which was obtained through a root locus study, additional feedback, and sensor mixing, as follows.

Root Locus

The root locus with $zte - zle$ feedback through the $10/(s + 10)$ lag filter with increasing gain $KR = 0, 500, \ldots, 2500$, is shown in Fig. 6 (at left), which indicates that the stabilization was due to increased pitch mode damping and a lowered plunge mode frequency. In Fig. 6, the arrows indicate increasing gain. The closed-loop roots of pitch, plunge, and filter modes with $KR = 500$ are denoted by the square symbol. The root-locus plot at right shows the effect of an additional feedback of $zte - zle$ through another $5/(s + 5)$ lag filter (see also Fig. 7) with $KR = 500$ and increasing gain $KP = 0, 500, \ldots, 2500$. This was equivalent to feedback of both pitch-angle and pitch-rate proportional signal. The closed-loop roots of pitch, plunge, and filter modes with $KR = 500$ and $KP = 1$ (denoted by square symbol), indicate a slight increase in pitch mode frequency and plunge mode damping. This feedback strategy resulted in increased pitch and plunge modal damping and separated their frequencies further.

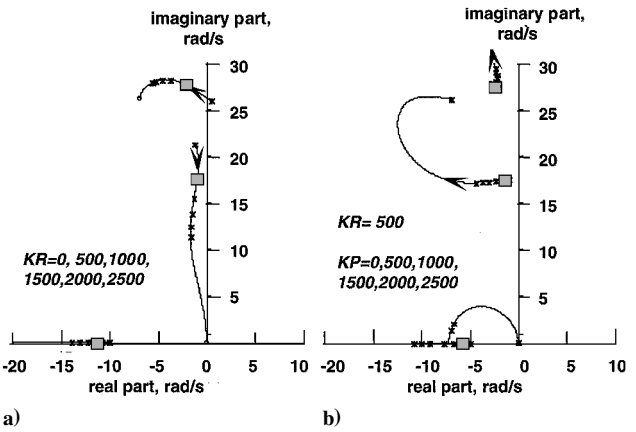

Fig. 6 a) Root-locus with $zte - zle$ feedback through a $10/(s+10)$ lag filter, with increasing gain KR (at left). b) Root-locus with additional pitch-rate feedback through a $5/(s+5)$ lag filter with KR = 500 and increasing gain KP.

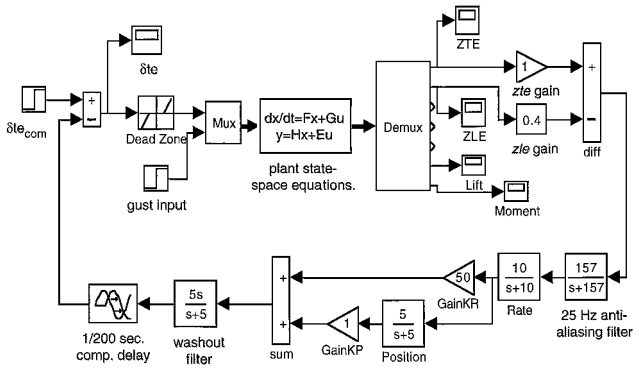

Fig. 7 Block diagram for numerical simulation of the digital control system implementation using the final classical control law 3 for flutter suppression.

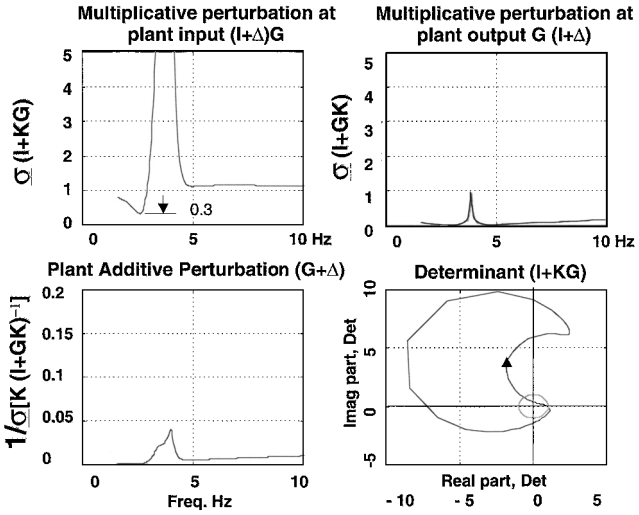

Fig. 8 Singular value plots for analysis of multivariable stability margins with a perturbation Δ, at the plant input or output, using classical control law 2, in air at 225 psf.

Pitch and Pitch-Rate Feedback Control Law

From the root-locus study, the feedback gains were selected as $KR = 500$ and $KP = 1$. This initial second-order pitch and pitch-rate feedback control law, as shown in Eq. (2), is denoted by law 2:

$$\delta te = [10/(s + 10)]\{500 + [5/(s + 5)]\}(zte - zle) \qquad (2)$$

The control law inputs *zte* and *zle* are in units of gravitational acceleration and the output δte is in degrees. The high feedback gain *KR* was required because the maximum $zte - zle$ signal was only of the order 0.05 *g*/deg. However, the high gain resulted in a severe robustness problem with respect to plant perturbation and individual sensor uncertainty. Singular value plots for analysis of multivariable stability margins[8,9] with a perturbation Δ, at the plant input or output, using control law 2, in air at 225 psf, are shown in Fig. 8. Here $\boldsymbol{G}(s)$ and $\boldsymbol{K}(s)$ denote plant and controller transfer matrices, and Δ denotes an unstructured uncertainty block, respectively. The two plots at top in Fig. 8 indicate that the minimum singular value $\underline{\sigma}(\boldsymbol{I} + \boldsymbol{KG})$ is only 0.3 at plant input and $\underline{\sigma}(\boldsymbol{I} + \boldsymbol{GK})$ is only 0.01 at plant output. Thus, at 225-psf dynamic pressure, the closed-loop system has very little robustness to a multiplicative perturbation Δ, with a magnitude above 0.01, at plant output. The singular value $1/\underline{\sigma}[\boldsymbol{K}(\boldsymbol{I} + \boldsymbol{GK})^{-1}]$ is only about 0.005 *g*/deg near 2 Hz, as shown in the lower left plot. This means that the plant has very little tolerance to an additive plant perturbation Δ, with a magnitude above 0.005 *g*/deg. The complex determinant locus of $(\boldsymbol{I} + \boldsymbol{KG})$ is shown at lower right. The minimum distance of the loci from the origin, which is a measure of its closeness to singularity, is only 0.3.

These singular value plots of $\underline{\sigma}(I + KG)$ can also be related to multivariable gain and phase margins using the universal gain and phase margin diagram[8,9] shown in Fig. 9. For example, minimum singular value $\underline{\sigma}(\boldsymbol{I} + \boldsymbol{KG})$ of 0.3 is equivalent to ±3-dB gain margin, that is, intersection of a horizontal line at $\underline{\sigma}(\boldsymbol{I} + \boldsymbol{KG}) = 0.3$ with parametric curve of $\underline{\sigma}(\boldsymbol{I} + \boldsymbol{KG})$ labeled 0 deg, or ±18-deg phase margin at the plant input, that is, the intersection of a horizontal line at $\underline{\sigma}(\boldsymbol{I} + \boldsymbol{KG}) = 0.3$ with the vertical axis.

Final Pitch and Pitch-Rate Feedback Control Law

This lack of robustness associated with this pitch and pitch-rate feedback control law was alleviated by selecting a feedback of a proper linear combination of the two sensors with lower gains for *KR*, instead of using their difference $(zte - zle)$. The linear combination of *zte* and *zle*, which is equivalent to feeding back both pitch acceleration $(zte - zle)$ and plunge acceleration $(zte + zle)$ in the ratio $0.7(zte - zle) + 0.3(zte + zle)$, appeared to provide a superior robust control law. The final classical feedback control law, using this combination that is equivalent to $(zte - 0.4zle)$ feedback, along with reduced gains of $KR = 50$ and $KP = 1$, was analyzed and implemented. This simple control is shown in Eq. (3) and is denoted by classical control law 3. The control law inputs *zte* and *zle* are in units of gravitational acceleration, and the output δte is in degrees:

$$\delta te = [10/(s + 10)]\{50 + [5/(s + 5)]\}(zte - 0.4zle) \qquad (3)$$

Response and Robustness Analysis

The closed-loop transient responses due to 1-deg step deflection of δte_{com}, in air at 225 psf, is shown in Fig. 10. The trailing-edge control surface response has only a 0.25-deg overshoot with a maximum rate of 12 deg/s, as shown by the two upper plots. The lift force plot, shown at lower left, indicates a 20% reduction of the overshoot, compared to the open-loop initial transient values shown

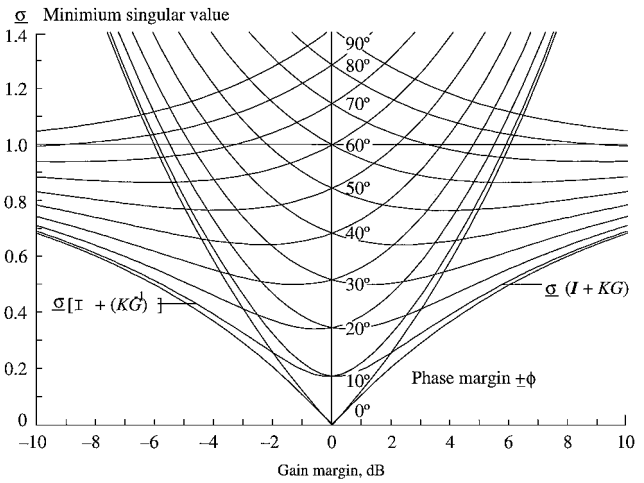

Fig. 9 Universal gain and phase margin analysis diagram.

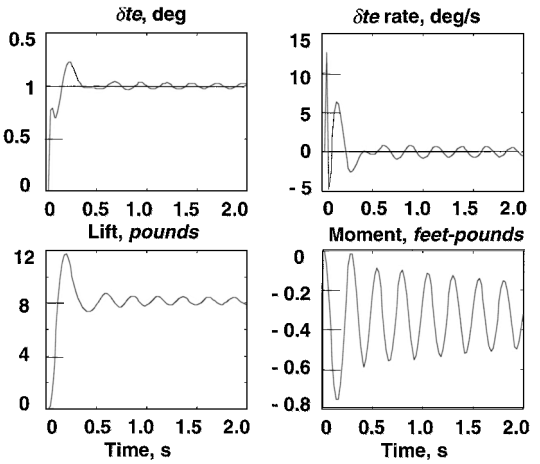

Fig. 10 Closed-loop responses: control surface deflection and rate, lift, and pitching moment due to step input δte using control law 3, in air at 225 psf.

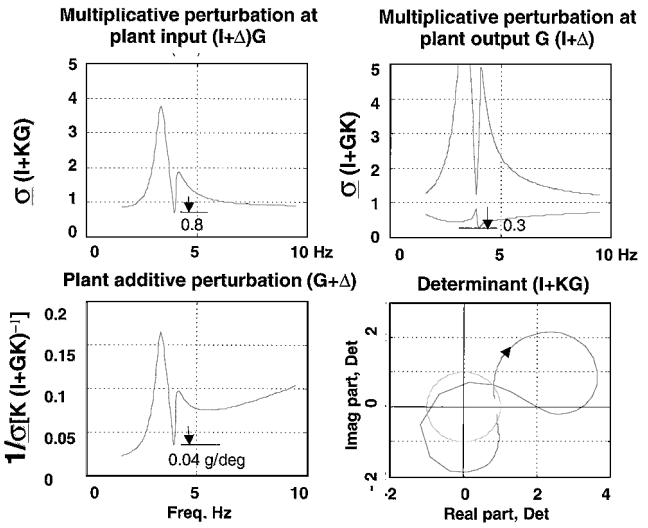

Fig. 11 Singular value plots for analysis of multivariable stability margins to perturbation Δ, using classical control law 3, in air at 225 psf.

in Fig. 3. The pitching moment, shown at lower right, converges to a small value of −0.3 ft · lb. Figure 11 shows the singular-value plots for analyzing the system stability margins[8,9] with law 3, at 225 psf dynammic pressure, in air. Here $\boldsymbol{G}$, $\boldsymbol{K}$, and Δ denote plant, controller, and uncertainty block transfer function, respectively. The two upper plots indicate that the minimum singular value $\underline{\sigma}(\boldsymbol{I}+\boldsymbol{KG})$ is increased to 0.8 and $\underline{\sigma}(\boldsymbol{I}+\boldsymbol{GK})$ is increased to 0.3, compared to the corresponding values of 0.3 and 0.01, respectively, with law 2 (see Fig. 8). The minimum singular value $\underline{\sigma}(\boldsymbol{I}+\boldsymbol{KG})$ of 0.8 is equivalent to −5 dB and 12 dB gain margins or ±45-deg phase margins at the plant input. These gain and phase margins are determined from Fig. 9 as described earlier. The minimum singular value $1/\underline{\sigma}[K(I+GK)^{-1}]$ is also increased to 0.04 *g*/deg near flutter frequency (lower left plot, compared to 0.005 *g*/deg with law 2, in Fig. 8), thus increasing the plant's tolerance to additive plant perturbation. The complex determinant loci of $(\boldsymbol{I}+\boldsymbol{KG})$, shown at lower right, has a minimum distance of 0.8 from the origin (compared to 0.3, for law 2). This robustness analysis indicates that the closed-loop system with law 3 has significantly higher multivariable stability margins, even at a high dynamic pressure of 225 psf.

Minimax Design

Flutter suppression control law design using a unified linear quadratic Gaussian and minimax method[10–12] is described next. The minimax approach is based on the steady-state differential game theory[11,12] and is analogous to the time domain H-infinity theory.[12–14] The minimax formulation is briefly presented next (see Refs. 10–12 for detailed derivation).

Let the state-space Eqs. (4–6) represent an nth-order linear system with control input $u(t)$, disturbance $w(t)$, design output $\boldsymbol{y}_d$, and sensor output $\boldsymbol{y}_s$, where all necessary rank, controllability, and observability conditions are assumed to be satisfied. Thus, we have, for the plant state-space equations,

$$\frac{\mathrm{d}\boldsymbol{x}(t)}{\mathrm{d}t} = \boldsymbol{F}\boldsymbol{x}(t) + \boldsymbol{G}\boldsymbol{u}(t) + \boldsymbol{G}_w\boldsymbol{w}(t), \qquad \boldsymbol{x}(0) = \boldsymbol{x}_0 \tag{4}$$

for the design output,

$$\boldsymbol{y}_d(t) = \boldsymbol{H}_d\boldsymbol{x}(t) + \boldsymbol{E}_{du}\boldsymbol{u}(t) \tag{5}$$

and for the sensor output,

$$\boldsymbol{y}_s(t) = \boldsymbol{H}_s\boldsymbol{x}(t) + \boldsymbol{E}_{sw}\boldsymbol{w}(t) \tag{6}$$

The minimax problem is to determine the plant input $u(t)$ that would minimize the quadratic performance index J and to find the worst plant disturbance $w(t)$ and initial condition x_0 that would maximize J defined in Eq. (7),

$$J = \frac{1}{2}\int_0^\infty \left(\boldsymbol{x}^T\boldsymbol{Q}_x\boldsymbol{x} + 2\boldsymbol{x}^T\boldsymbol{Q}_{xu}\boldsymbol{u} + \boldsymbol{u}^T\boldsymbol{Q}_u\boldsymbol{u}\right)\mathrm{d}t \tag{7}$$

subject to the constraint Eq. (4) with $\boldsymbol{x}_0\boldsymbol{x}_0^T = \boldsymbol{X}_0$ and a specified W defined by

$$W = \frac{1}{2}\int_0^\infty \left(\boldsymbol{w}^T\boldsymbol{R}_w\boldsymbol{w}\right)\mathrm{d}t \tag{8}$$

When we used the calculus of variation with respect to $x(t)$, $u(t)$, $\boldsymbol{w}(t)$ and a vector Lagrange multiplier $\lambda(t)$, the conditions for $\partial J = 0$, the equations for the linear quadratic minimax state feedback regulator were obtained. These equations were derived in Refs. 10 and 11. The basic equations are presented here. The significance of the cross-weighting matrix $\boldsymbol{Q}_{xu}$ in Eq. (7) and how it can be selected for pole placement of the state regulator will be shown later in the state feedback regulator design subsection.

State Feedback Regulator Equations

The steady-state feedback regulator equations are given by Eqs. (9–11):

$$\boldsymbol{u} = -\boldsymbol{C}_0\boldsymbol{x} \tag{9}$$

where $\boldsymbol{C}_0 = -\boldsymbol{Q}_u^{-1}\left(\boldsymbol{G}^T\boldsymbol{S} + \boldsymbol{Q}_{xu}^T\right)$ and

$$\boldsymbol{w} = \boldsymbol{C}_w\boldsymbol{x} \tag{10}$$

where $\boldsymbol{C}_w = \gamma^{-2}\boldsymbol{R}_w^{-1}\boldsymbol{G}_w^T\boldsymbol{S}$ and where γ is an arbitrary scalar design parameter and the $n \times n$ matrix $\boldsymbol{S}$ is the solution of the steady-state regulator Riccati equation (11)

$$\boldsymbol{S}\boldsymbol{F} + \boldsymbol{F}^T\boldsymbol{S} + \boldsymbol{Q}_x - (\boldsymbol{S}\boldsymbol{G} + \boldsymbol{Q}_{xu})\boldsymbol{Q}_u^{-1}(\boldsymbol{S}\boldsymbol{G} + \boldsymbol{Q}_{xu})^T + \boldsymbol{S}\left(\gamma^{-2}\boldsymbol{G}_w\boldsymbol{R}_w^{-1}\boldsymbol{G}_w^T\right)\boldsymbol{S} = \boldsymbol{0} \tag{11}$$

where $\boldsymbol{\lambda} = \boldsymbol{S}\boldsymbol{x}$. The positive-definite symmetric steady-state solution for S can also be obtained from the $(2n \times n)$ eigenvectors of the n stable eigenvalues of the Hamiltonian matrix

$$\begin{bmatrix} \left(\boldsymbol{F} - \boldsymbol{G}\boldsymbol{Q}_u^{-1}\boldsymbol{Q}_{xu}^T\right) & \left(-\boldsymbol{G}\boldsymbol{Q}_u^{-1}\boldsymbol{G}^T + \gamma^{-2}\boldsymbol{G}_w\boldsymbol{R}_w^{-1}\boldsymbol{G}_w^T\right) \\ -\left(\boldsymbol{Q}_x + \boldsymbol{Q}_{xu}\boldsymbol{Q}_u^{-1}\boldsymbol{Q}_{xu}^T\right) & -\left(\boldsymbol{F} - \boldsymbol{G}\boldsymbol{Q}_u^{-1}\boldsymbol{Q}_{xu}^T\right)^T \end{bmatrix} \tag{12}$$

If all of the eigenvectors are partitioned into two $n \times n$ matrices $\underline{\boldsymbol{X}}$ and $\underline{\boldsymbol{\Lambda}}$ that represent the stable subspace eigenvectors of x and λ, respectively, then $\boldsymbol{S} = \underline{\boldsymbol{X}}^{-1}\underline{\boldsymbol{\Lambda}}$. Substituting the constant optimal state feedback gains, $\boldsymbol{C}_o$ and $\boldsymbol{C}_w$, in Eq. (4), the closed-loop state feedback system is given by

$$\frac{\mathrm{d}\boldsymbol{x}}{\mathrm{d}t} = [\boldsymbol{F} + \boldsymbol{G}_w\boldsymbol{C}_w + \boldsymbol{G}\boldsymbol{C}_o]\boldsymbol{x}, \qquad \boldsymbol{x}(0) = \boldsymbol{x}_0 \tag{13}$$

Using Eqs. (4), (11), and (13), it can be shown[10,11] that with this state feedback regulator, the minimax J and W defined in Eqs. (7) and (8) are given by

$$J = 0.5\ \mathrm{tr}\,[\boldsymbol{S}\boldsymbol{X}_0] + \gamma^2\boldsymbol{W} \tag{14}$$

$$W = 0.5\ \mathrm{tr}\left[\boldsymbol{C}_w^T\boldsymbol{R}_w\boldsymbol{C}_w\boldsymbol{X}\right] \tag{15}$$

where $\boldsymbol{X}$ is the solution of the Lyapunov equation (16) and $\boldsymbol{X}_0 = [\boldsymbol{x}(0)\boldsymbol{x}(0)^T]$:

$$[\boldsymbol{F} + \boldsymbol{G}_w\boldsymbol{C}_w + \boldsymbol{G}\boldsymbol{C}_o]\boldsymbol{X} + \boldsymbol{X}[\boldsymbol{F} + \boldsymbol{G}_w\boldsymbol{C}_w + \boldsymbol{G}\boldsymbol{C}_o]^T + \boldsymbol{x}(0)\boldsymbol{x}(0)^T = [0] \tag{16}$$

The worst $x(0)$ that maximizes J is given by the eigenvector of the maximum eigenvalue of S. The standard linear quadratic regulator (LQR) solution is obtained when $\gamma = \infty$, that is, $\boldsymbol{C}_w = 0$.

State-Estimator Equations

The derivation of coupled state-estimator equations using a linear quadratic minimax approach was presented in Ref. 12. The equivalent state-space solutions of the H-infinity problem were presented in Refs. 13 and 14. The state-estimator gain $\boldsymbol{B}_0\boldsymbol{D}_0$ is obtained by finding the symmetric positive-definite solution for $\boldsymbol{P}$ from the steady-state estimator Riccati equation (19):

$$\boldsymbol{B}_0 = -\left(\boldsymbol{P}\boldsymbol{H}_s^T + \boldsymbol{R}_{wv}\right)\boldsymbol{R}_v^{-1} \tag{17}$$

$$\boldsymbol{D}_0 = (\boldsymbol{I} - \gamma^{-2}\boldsymbol{P}\boldsymbol{S})^{-1} \tag{18}$$

where $\rho(\boldsymbol{P}\boldsymbol{S}) < \gamma^2$,

$$\boldsymbol{P}\boldsymbol{F}^T + \boldsymbol{F}\boldsymbol{P} + \boldsymbol{G}_w\boldsymbol{R}_w\boldsymbol{G}_w^T - \left(\boldsymbol{P}\boldsymbol{H}_s^T + \boldsymbol{R}_{wv}\right)\boldsymbol{R}_v^{-1}\left(\boldsymbol{P}\boldsymbol{H}_s^T + \boldsymbol{R}_{wv}\right)^T + \boldsymbol{P}(\gamma^{-2}\boldsymbol{Q}_x)\boldsymbol{P} = \boldsymbol{0} \tag{19}$$

Here, $\boldsymbol{R}_v = \boldsymbol{E}_{sw}\boldsymbol{R}_w\boldsymbol{E}_{sw}^T$ and must be positive definite and $\boldsymbol{R}_{wv} = \boldsymbol{G}_w\boldsymbol{R}_w\boldsymbol{E}_{sw}^T$. In Eq. (18) the spectrum $\rho[\boldsymbol{P}\boldsymbol{S}]$ must be less than γ^2 for $\boldsymbol{D}_0$ to exist. The positive-definite symmetric steady-state solution for $\boldsymbol{P}$ in Eq. (19) can also be obtained from the $(2n \times n)$ eigenvectors of the n stable eigenvalues of the estimator Hamiltonian matrix,

$$\begin{bmatrix} \left(\boldsymbol{F} - \boldsymbol{R}_{wv}\boldsymbol{R}_v^{-1}\boldsymbol{H}_s\right)^T & \left(-\boldsymbol{H}_s^T\boldsymbol{R}_v^{-1}\boldsymbol{H}_s + \gamma^{-2}\boldsymbol{H}_d^T\boldsymbol{Q}_{yd}^{-1}\boldsymbol{H}_d\right) \\ -\boldsymbol{G}_w\boldsymbol{R}_w\boldsymbol{G}_w^T - \boldsymbol{R}_{wv}\boldsymbol{R}_v^{-1}\boldsymbol{R}_{wv}^T & -\left(\boldsymbol{F} - \boldsymbol{R}_{wv}\boldsymbol{R}_v^{-1}\boldsymbol{H}_s\right) \end{bmatrix} \tag{20}$$

If all of the eigenvectors of Eq. (20) are partitioned into two $(n \times n)$ matrices $\underline{\boldsymbol{X}}$ and $\underline{\boldsymbol{\Lambda}}$, then $\boldsymbol{P} = \underline{\boldsymbol{X}}^{-1}\underline{\boldsymbol{\Lambda}}$. The state-estimate vector z is given by

$$\frac{\mathrm{d}z}{\mathrm{d}t} = \boldsymbol{F}z + \boldsymbol{G}_w\boldsymbol{w} + \boldsymbol{G}\boldsymbol{u} + \boldsymbol{D}_0\boldsymbol{B}_0(\boldsymbol{H}_s z - \boldsymbol{y}_s) \tag{21}$$

Controller Equations

Substituting Eqs. (9), (10), (17), and (18) in Eq. (21), the state-estimation feedback controller Eqs. (22) and (23) are obtained. The standard linear-quadratic Gaussian controller is obtained when $\gamma = \infty$:

$$\frac{\mathrm{d}z}{\mathrm{d}t} = [\boldsymbol{A}_0]z - [\boldsymbol{D}_0\boldsymbol{B}_0]\boldsymbol{y}_s \tag{22}$$

$$\boldsymbol{u} = [\boldsymbol{C}_o]z \tag{23}$$

where $[\boldsymbol{A}_0] = [\boldsymbol{F} + \boldsymbol{G}_w\boldsymbol{K}_w + \boldsymbol{G}\boldsymbol{C}_o + \boldsymbol{D}_0\boldsymbol{B}_0\boldsymbol{H}_s]$.

Design Procedure

In this design, the output $\boldsymbol{y}_d$ was treated as a scalar and chosen to be the same linear combination of the trailing- and leading-edge accelerometer output ($zte - 0.4zle$) as used in the final classical design. One advantage of this choice was that the plant had no transmission zeros in the open right-half s plane. Usually in a frequency domain H-infinity design, the plant equations are augmented with weighting transfer functions. In this time-domain formulation, the weights were chosen as constants. These weighting constants are chosen as the inverse of the desired magnitude of the weighted quantities. The initial controller was designed with a large value of $\gamma^2 = 500$, using the reduced fourth-order plant Eqs. (4–6), in air at 225 psf, assuming $\boldsymbol{G}_w = \boldsymbol{G}$. The block diagram for this iterative design procedure is shown in Fig. 12. The detailed design steps are described next.

State Feedback Regulator Design

The average output of the accelerometer sensors were of the order 0.1 g, (see Fig. 4), and control surface maximum rms deflection was desired to be of the order 1 deg. Thus, the initial values of the weighting matrices were chosen as follows: $Q_{ys} = 100$, $\boldsymbol{Q}_x = [\boldsymbol{H}_s^T\boldsymbol{Q}_{ys}\boldsymbol{H}_s]$, and $\boldsymbol{Q}_u = 1.0$. Instead of setting the cross-weighting matrix $\boldsymbol{Q}_{xu} = [0]$ as usual practice, the cross-weighting matrix $\boldsymbol{Q}_{xu}$ was selected to place all state-regulator poles beyond a certain distance $\alpha = 3$ rad/s to the left of imaginary axis, by using

$$\boldsymbol{Q}_{xu} = -\alpha\boldsymbol{G}(\boldsymbol{G}^T\boldsymbol{G})^{-1}\boldsymbol{Q}_u \tag{24}$$

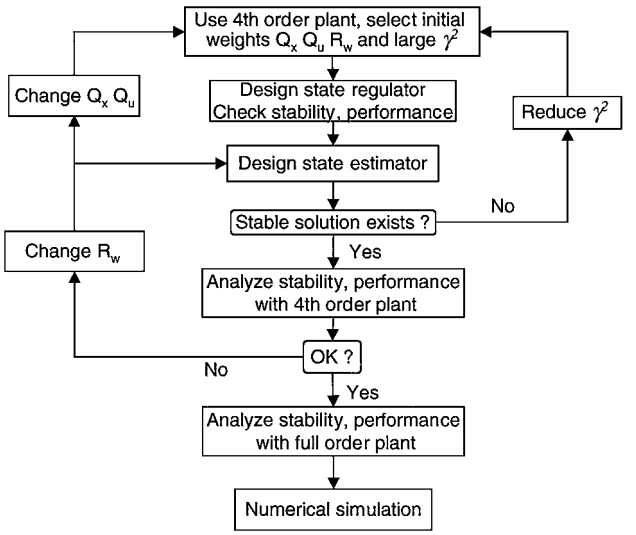

Fig. 12 Block diagram of iterative procedure for minimax control law design and evaluation.

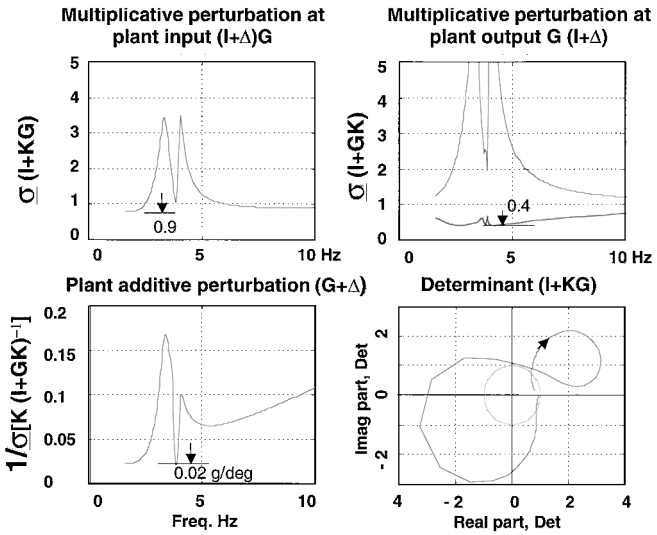

Fig. 13 Singular value plots for analysis of multivariable stability margins using minimax control law 4, in air at 225 psf.

Thus, if $(\boldsymbol{G}^T\boldsymbol{G})^{-1}$ exists, $\boldsymbol{G}\boldsymbol{Q}_u^{-1}\boldsymbol{Q}_{xu} = -\alpha\boldsymbol{I}$, and eigenvalues of the diagonal matrix block in Eq. (12) are offset by $-\alpha\boldsymbol{I}$, resulting in a more stable system. The control-weighting matrix $\boldsymbol{Q}_u$ was also subsequently reduced from 1.0 to 0.01 after a few design cycles to improve the regulator performance. This process of reducing $\boldsymbol{Q}_u$ is equivalent to the asymptotic state-estimator loop-transfer recovery.

State-Estimator Design

The state estimator was designed as a dual to the state regulator with $\boldsymbol{R}_w = 1$, each diagonal elements of $\boldsymbol{R}_v = 0.01$ and $\boldsymbol{R}_{wv} = [0]$. The performance of the control law was then examined with the full-order plant. After a few design cycles, $\boldsymbol{R}_w$ was increased to 36 to improve system robustness. Because we also choose $\boldsymbol{G}_w = \boldsymbol{G}$, this increase was equivalent to the asymptotic state-regulator loop-transfer recovery process.

Fourth-Order Minimax Control Law

Subsequent solutions to the state regulator and state estimator were obtained with the same choice of weighting matrices, with decreasing value of γ^2, for which positive-definite solutions for S and P could be obtained. The fourth-order minimax control law was designed with $\gamma^2 = 50$ to obtain a low bandwidth controller. Note that feasible solutions could be obtained for even lower values of γ^2 up to $\gamma^2 > \rho(\boldsymbol{P}\boldsymbol{S})$, below which the disturbance authority would exceed the control authority.

Figure 13 shows key singular value plots used for analysis of multivariable stability margins relative to multiplicative and additive

perturbations Δ at the plant input and output, with the minimax control law 4. The upper two plots show that the minimum singular value $\underline{\sigma}(\boldsymbol{I} + \boldsymbol{KG})$ is increased to 0.9 and $\underline{\sigma}(\boldsymbol{I} + \boldsymbol{GK})$ is increased to 0.4 (compared to the corresponding values of 0.8 and 0.3 for control law 3, shown in Fig. 11). However, the minimum singular value $1/\underline{\sigma}[\boldsymbol{K}(\boldsymbol{I} + \boldsymbol{GK})^{-1}]$ is reduced to 0.02 g/deg near flutter frequency (lower left plot, compared to 0.04 g/deg with law 3, in Fig. 11), The complex determinant loci of $(\boldsymbol{I} + \boldsymbol{KG})$, shown at lower right, has a minimum distance of 0.9 from the origin (compared to 0.8, for law 3). Although control law 4 was slightly more robust than the classical control law 3 in Eq. (3), it was more complex and sensitive to the plant model accuracy. The simpler control law 3 provided better damping with lower control surface activity and was implemented and tested in the wind tunnel after extensive numerical simulation.

Numerical Simulation

Before the wind-tunnel test entry, the digital implementation was numerically simulated using MATLAB®/Simulink software. The performance and robustness of the final design was analyzed using the analytical 14th-order plant state-space equations. The block diagram for numerical simulation of the digital control system using the final classical control law 3 is shown in Fig. 7. The block diagram shows additional filters required for digital implementation. Two first-order 25-Hz antialiasing filters $157/(s + 157)$ were added to the plant sensor output. A washout filter $5s/(s + 5)$ and one-cycle computational delay were appended to the controller output. The 1/200-s computational delay was modeled by a $(400 - s)/(400 + s)$ filter. This simulation also included the nonlinear effects of a deadband present in the electrohydraulic actuator. Application of the upper and lower spoiler for transonic flutter suppression with the same digital control law was also investigated using similar numerical simulation.

Flutter Suppression Test Results

The active flutter suppression control law 3 was successfully tested in air and in a heavy gas medium in the NASA Transonic Dynamics Tunnel at speeds up to Mach 0.95 . The wind-tunnel test results indicated an increase in the flutter instability boundary from the open-loop dynamic pressure of 150 psf to the tunnel limit of 200 psf at Mach 0.77 in a heavy gas medium. Major flutter suppression test points at a set of Mach numbers and dynamic pressures in a heavy gas medium are shown in Fig. 14. The solid line indicates the estimated experimental flutter boundary, as determined from wind-tunnel tests, in heavy gas. This boundary exhibits a typical but a broad transonic flutter bucket, a gradual drop in flutter dynamic pressure starting at Mach 7.0, then a sharp rise after Mach 0.8. The test points below the estimated flutter boundary represent both open-loop and closed-loop tests using control law 3. The points above the flutter boundary represent closed-loop tests using control law 3. The tests at Mach 0.8 indicated an increase in the flutter stability boundary from the open-loop dynamic pressure of 145 psf to the tunnel upper limit of 200 psf, an increase of over 50%. The classical control law 3 provided superior performance and was demonstrated to be stable over a multiplicative gain variation from 0.25 (−12 dB) to 7 (16 dB), and phase variation from −90 to +60 deg at 195 psf. The analytical predictions were of the order from −5 to 12-dB gain margins and ±45-deg phase margins, indicating that the singular-value-based phase and gain margin predictions are generally conservative.[8] Comparison of open-loop and closed-loop rms responses of the trailing-edge accelerometer and control surface using the classical control law 3 are shown in Figs. 15 and 16, respectively. Figure 15 indicates that when the system is open-loop stable, closing the loop actually alleviates the load by 30%. The closed-loop rms response of the trailing-edge inboard accelerometer near 195-psf dynamic pressures were of the order of 0.035 g. The analytical predictions, based on the linear state-space model and a Dryden gust model with 6-in./s rms gust, were also of the order 0.035 g. Figure 16 indicates that the classical control law 3 generally requires maximum rms control surface deflection of the order 0.3 deg. The analytical predictions, based on the linear state-space model with 6-in./s rms gust, were of the order 0.66 deg. The higher predictions may be due to the lack of an accurate analytical model at transonic speed. Another set of optimal control laws designed by Waszak[15] were also tested successfully. These control laws used upper and lower spoilers as control surfaces for flutter suppression. Performances of these control laws with those of the present classical control law 3 are compared in Ref. 15.

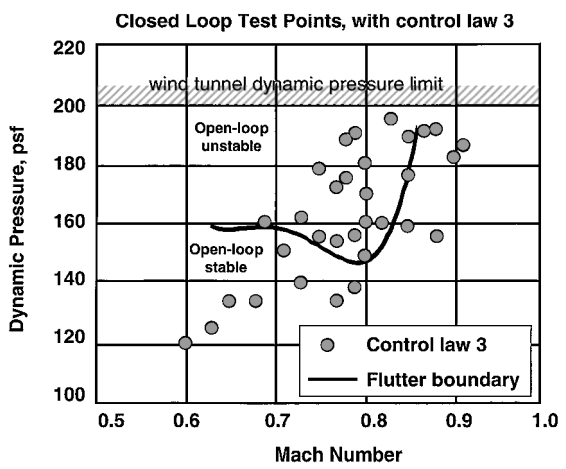

Fig. 14 Open-loop flutter boundary and closed-loop flutter suppression results from wind-tunnel tests in heavy gas.

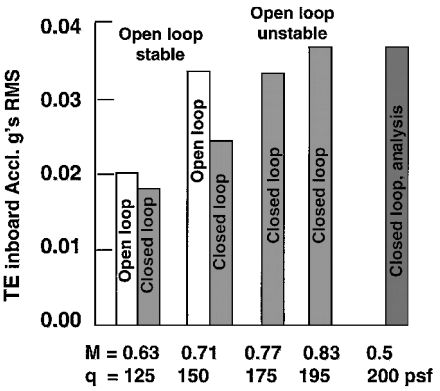

Fig. 15 Open-loop and closed-loop rms responses using classical control law 3, from wind-tunnel tests in heavy gas medium.

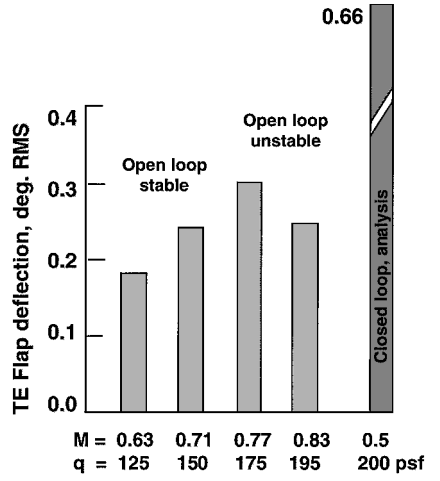

Fig. 16 Control surface rms responses using the classical control law 3, from wind-tunnel tests in heavy gas medium.

Conclusions

A simple classical robust control law was designed based on physical principles and was digitally implemented to successfully suppress flutter in transonic flow. A comparable robust control law was also designed using the minimax technique. Analysis and

improvement of stability robustness for this multivariable system with respect to unstructured perturbations at the plant, input, and output were important steps in such a design process. In wind-tunnel tests in air and a heavy gas medium, the closed-loop flutter dynamic pressure was increased by over 50% to the tunnel upper limit. The control law exhibited significant robustness to gain and phase perturbations, even in the presence of oscillating shocks and flow separation.

Acknowledgments

The author wishes to acknowledge Martin R. Waszak, Robert C. Scott, Sherwood T. Hoadley, Carol D. Wieseman, Robert M. Bennett, Robert K. Sleeper, Michael H. Durham, Jose A. Rivera Jr., and the rest of the benchmark active control technology project team, without whose help this work would not be possible.

References

[1]Bennett, R. M., Eckstrom, C. V., Rivera, J. A., Jr., Dansberry, B. E., Farmer, M. G., and Durham, M.H., "The Benchmark Aeroelastic Models Program—Description and Highlights of Initial Results," NASA TM 104180, 1991.

[2]Rivera, J. A., Jr., Dansberry, B. E., Farmer, M. G., Eckstrom, C. V., Seidel, D. A., and Bennett, R. M., "Experimental Flutter Boundaries with Unsteady Pressure Distribution for the NACA 0012 Benchmark Model," AIAA Paper 91-1010, April 1991; also NASA TM-104072, 1991.

[3]Rivera, J. A., Jr., Dansberry, B. E., Bennett, R. M., Durham, M. H., and Silva, W. A., "NACA 0012 Benchmark Model Experimental Flutter Results with Unsteady Pressure Distribution," AIAA Paper 92-2396, April 1992; also NASA TM-107581, 1992.

[4]Durham, M. H., Keller, D. F., Bennett, R. M., and Wieseman, C. D., "A Status Report on a Model for Benchmark Active Control Testing," AIAA Paper 91-1011, April 1991.

[5]Hoadley, S. T., and Adams, W. M., Jr., "ISAC—Interaction Structures, Aerodynamics, and Controls. Version 5.1 Sample Cases with Guides for UNIX Operating Systems," NASA TM-100667, 1992.

[6]Mukhopadhyay, V., "Flutter Suppression Control Law Design and Testing for the Active Flexible Wing," *Journal of Aircraft*, Vol. 32, No. 1, 1995, pp. 45–51.

[7]Perry, B., III, Cole, S. R., and Miller, G. D., "A Summary of an Active Flexible Wing Program," *Journal of Aircraft*, Vol. 32, No. 1, 1995, pp. 10–15.

[8]Mukhopadhyay, V., "Stability Robustness Improvement Using Constrained Optimization Techniques," *Journal of Guidance, Control, and Dynamics*, Vol. 10, No. 2, 1987, pp. 172–177.

[9]Pototzky, A. S., Wieseman, C. D., Hoadley, S. T., and Mukhopadhyay, V., "On-Line Performance Evaluation of Multiloop Digital Control Systems," *Journal of Guidance, Control, and Dynamics*, Vol. 15, No. 4, 1992, pp. 878–884.

[10]Bryson, A. E., Jr., and Carrier, A. C., "A Comparison of Control Synthesis Using Differential Games (H-Infinity) and LQR," AIAA Paper 89-3598, Aug. 1989.

[11]El Ghaoui, L., Carrier, A. C., and Bryson, A. E., Jr., "Linear Quadratic Minimax Controllers," *Journal of Guidance, Control, and Dynamics*, Vol. 15, No. 4, 1992, pp. 953–951.

[12]Rhee, I., and Speyer, J. L., "A Game Theoretic Controller and Its Relationship to H-Infinity and Linear-Exponential-Gaussian Synthesis," *Proceedings of the 28th IEEE Conference on Decision and Control*, Inst. of Electrical and Electronics Engineers, 1989, pp. 909–915.

[13]Doyle, J. C., Glover, K., Khargonekar, P. P., and Frances, B. A., "State-Space Solutions to Standard H2 and H-Infinity Control Problems," *IEEE Transactions on Automatic Control*, Vol. 34, No. 8, 1989, pp. 831–847.

[14]Carrier, A. C., "State-Space Formulae for all the Stabilizing Discrete Controllers that Satisfy an H-Infinity Norm Bound," *International Journal of Control*, Vol. 16, No. 1, 1995, pp. 65–96.

[15]Waszak, M. R., "Robust Multivariable Flutter Suppression for the Benchmark Active Control Technology (BACT) Wind-Tunnel Model," *Journal of Guidance, Control, and Dynamics* (to be published).